THE JOURNAL OF PHYSICAL CHEMISTRY C
A JOURNAL OF THE AMERICAN CHEMICAL SOCIETY

pubs.acs.org/JPCC

Article

Porous Organic Cage CC3: An Effective Promoter for Methane Hydrate Formation for Natural Gas Storage

Shurraya Denning, Jolie M. Lucero, Ahmad A. A. Majid, James M. Crawford, Moises A. Carreon,* and Carolyn A. Koh*

Cite This: *J. Phys. Chem. C* 2021, 125, 20512−20521

Read Online

ACCESS | Metrics & More | Article Recommendations | Supporting Information

ABSTRACT: Herein, the synergistic effect of combining gas hydrates with a novel prototypical porous organic cage, denoted as CC3 (microporous crystalline structure with diamondoid pores), for methane storage is demonstrated using a high-pressure differential scanning calorimeter. Adding CC3 improved the extent of methane hydrate formation significantly, increasing the water-to-hydrate conversion from 4.5 to 87.5%, thus increasing the amount of methane stored relative to the water in the system from 0.42 to 8.1 mmol/g. The presence of CC3 also decreased the induction time consistently to 0.8 ± 0.1 h, whereas without CC3, hydrates only formed 30% of the time at 5.9 ± 3.9 h of induction time. This increase in conversion and decrease in induction time is attributed to CC3's large surface area, high methane adsorption, and reversible water uptake. A depression in the hydrate dissociation temperature by as much as 1.6 °C suggests hydrate formation occurred in the confined space in CC3, most likely in its void and interstitial spacing. CC3 displayed remarkable stability, recyclability, and enhanced performance in promoting methane hydrate formation to achieve a high capacity for methane storage.

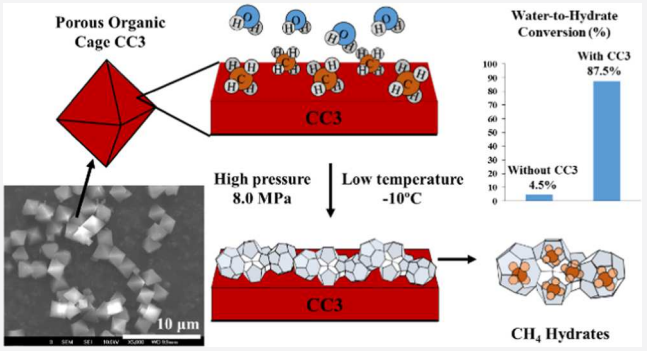

1. INTRODUCTION

The combustion of methane, the primary component of natural gas, is a relatively clean process when compared to some other fossil fuels and coal, making it a desirable energy source from an environmental standpoint.[1,2] To maximize the energy efficiency of natural gas, the gas must be effectively stored and transported, which can be difficult, as natural gas has a low density. The traditional strategies for storing and transporting natural gas come with various limitations: compressed natural gas is explosive in nature due to the high pressure;[3] liquefying natural gas is energy intensive due to the low temperatures required (111.2 K);[4] and underground facilities, such as depleted reservoirs or aquifers, are geologically and geographically limited.[5] Therefore, optimizing the storage and transportation of natural gas would be favorable both environmentally and economically.

The use of gas hydrates as a means of natural gas storage and transportation has been explored by independent research groups.[3,6−9] Gas hydrates consist of gas molecules, such as methane, trapped in cages made of water molecules connected via hydrogen bonds.[10] An illustration of a methane hydrate is displayed in Figure 1a.

Methane hydrates offer a potential 164-fold increase in storage density, as 1 m^3 of hydrate contains approximately 160 m^3 of methane at standard temperature and pressure (STP).[2,14] Gas hydrates are typically formed under high pressure and low-temperature conditions and are found occurring naturally in oceanic sediments.[15] Although methane hydrates typically require higher than ambient pressures to form, they can exhibit a unique anomaly called "self-preservation" that imparts ambient pressure stability at low temperatures.[16] Self-preservation is suggested to be the result of an ice layer forming on the outer surface of the hydrate, preventing gas from escaping, as the pressure is reduced to ambient while maintaining temperatures below the freezing point of ice.[7] This anomaly makes gas hydrates favorable for natural gas transportation.[17] Few studies have investigated the length of time a methane hydrate maintains stability at atmospheric temperatures, with results ranging from 3 months at −20 °C[18] to 2 years at −2 °C.[19]

To develop gas hydrates for methane storage and transportation, two prevailing barriers to hydrate formation must be addressed: (1) low water-to-hydrate conversion (wasted water potential) and (2) long induction times for hydrate nucleation (prolonged periods of high pressure). Mass transfer limitations

Received: May 27, 2021
Published: September 8, 2021

https://doi.org/10.1021/acs.jpcc.1c04657
J. Phys. Chem. C 2021, 125, 20512−20521

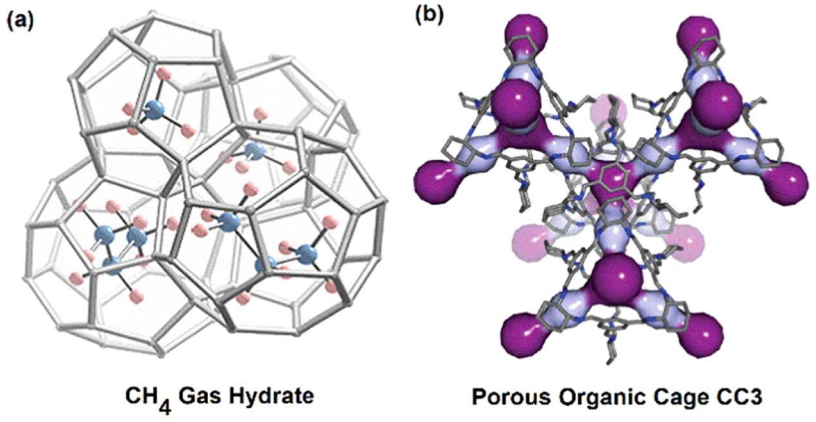

Figure 1. (a) Methane structure I hydrate, consisting of water molecules forming hydrogen bonds to encage methane. Unit cell length is ~12 Å.[11] (b) Porous organic cage CC3, consisting of 1,3,5-triformylbenzene coordinated with trans-1,2-diaminocyclohexane, displaying a limiting pore aperture of 3.6 Å in light purple and the internal cage cavity of ~5 Å in dark purple.[12,13]

negatively affect the water-to-hydrate conversion, as hydrates usually form at the interface of gas and water, thus creating a "hydrate film" that limits gas diffusion to the trapped water phase. Heat transfer limitations lead to slow hydrate nucleation induction times, as the local heat released by hydrate formation creates an unfavorable environment since low temperatures are needed for hydrate formation. The local structure of water molecules (i.e., water ordering) also affects hydrate formation. Addressing these issues could transition natural gas storage and transportation in hydrates into a commercialized process.

Three general approaches to address these issues are the use of chemical additives and porous materials (termed here as promoters) and apparatus design. Chemical additives typically target thermodynamic (shifting the stable region of hydrate formation to milder conditions) and/or kinetic (e.g., increase gas solubility in water, change water ordering) aspects of the hydrate formation process. Examples of employed chemical additives are: tetrahydrofuran (THF),[20] sodium dodecyl sulfate (SDS),[21] tetrabutylammonium bromide (TBAB),[22] tetrabutylammonium fluoride (TBAF),[23] trimethylene sulfide,[24] 1,3-dioxolane,[25] cyclopentane,[26] seawater,[27] methyl ester sulfonate,[28] leucine,[29] amino acids arginine, histidine, tryptophan,[30] fungus,[31] and β-cyclodextrin.[32] Apparatus designs typically target increasing the water-to-gas contact area but may also focus on other avenues such as removing the local heat of hydrate formation. Some of the apparatus designs that have been explored are unstirred tank,[33] semi-continuous stirred tank,[34] bubble column,[35] fixed bed reactor,[36] and heat transfer plates.[37] Porous materials are highly sought after due to their large surface areas increasing the gas-to-water contact area and unique chemistry influencing hydrate nucleation and growth. A few examples of porous materials studied are hollow silica,[38] silica gels,[39] silica sand,[40] glass beads,[36] carbon nanotubes,[41] activated carbon,[42−44] polyurethane foam,[45] metal organic frameworks,[46−52] and zeolites.[48,53−56] Physical characteristics, including pore size, structural geometry, and surface chemistry govern a materials' effect on hydrate growth performance.[57] A better understanding of porous materials and hydrate formation and dissociation structure-function relationships is key to determining the optimal promoter.

Despite the wide range of hydrate formation growth promoters studied, one understudied group is organic porous materials.[58] A novel class of organic porous materials that is highly appealing as a hydrate growth promoter is porous organic cages (POCs).[13] To the best of our knowledge, no studies have been conducted using any POC as a hydrate growth promoter. POCs exhibit a unique crystal structure, as they are covalently bonded discrete organic cages that can self-assemble into a microporous material.[13] This solid-state molecular packing is unlike other porous materials such as zeolites or activated carbon.[59,60] The resulting assembly has intrinsic pores (inside the cage) and extrinsic pores (between the assembled cages), and the structure contains the following covalent bonds: C-N, N-H, H-C, and C-C.[13]

The work reported here targets, specifically, the porous organic cage denoted as αCC3 (also referred to as CC3) as a methane hydrate growth promoter. This POC has a 3D microporous crystalline structure comprised of 1,3,5-triformylbenzene coordinated with trans-1,2-diaminocyclohexane that forms cages with a unimodal limiting pore size of ~3.6 Å and internal cavity diameter of ~5 Å.[12,13] These cages are connected via the cyclohexyl groups to form diamondoid pores, as illustrated in Figure 1b.[13] CC3 is being explored for various applications, such as gas adsorbent (SF_6, Xe;[61] acetylene, ethane, CH_4, ethylene;[62] CO_2[63]), proton conductor,[64] gas chromatography separations with chiral alcohols,[65] catalytic support for noble metals,[66] and for gas separation via membranes.[67−69]

CC3 possesses several unique and advantageous properties that make this microporous crystalline material highly appealing as a methane hydrate promoter. These properties include large surface area,[13] high methane uptake,[58] flexible framework,[63] stability under high pressure,[62,63] and chemical stability.[69] In principle, these properties would not only enable CC3 to improve water-to-hydrate conversion and reduce hydrate nucleation induction time but also could result in high recyclability of CC3.

In this work, we studied the impact of CC3 on methane hydrate formation and dissociation by employing a high-pressure differential scanning calorimeter (HP-DSC). The addition of CC3 improved the water-to-hydrate conversion significantly and reduced the hydrate nucleation induction time primarily due to the large surface area and high methane adsorption.

2. EXPERIMENTAL METHODS

The microwave-assisted thermal treatment was used to synthesize uniform and narrow size distribution CC3 crystals.

https://doi.org/10.1021/acs.jpcc.1c04657
J. Phys. Chem. C 2021, 125, 20512−20521

The microwave-assisted approach is an effective synthetic strategy to synthesize chemically diverse porous crystals with a narrow size distribution,[70,71] including CC3 crystals.[72]

The precursors used in the CC3 synthesis were 1,3,5-triformylbenzene (ACROS Organics, 98%), (±)-trans-1,2-diaminocylcohexane (Sigma-Aldrich, 99%), dichloromethane (ACS-certified, stabilized, Fisher Scientific), and trifluoroacetic acid (AlfaAesar, 99%). In a typical synthesis, 25 mL of dichloromethane was added slowly to 200 mg of 1,3,5-triformylbenzene in a Teflon liner. Next, 100 μL of trifluoroacetic acid was added. In a separate beaker, 25 mL of dichloromethane was added to 102 mg of (±)-trans-1,2-diaminocylcohexane. This solution was slowly added to the solution in the Teflon liner before putting the liner into an XP1500 vessel. The vessel was placed in a CEM Mars 5 microwave and a thermocouple was introduced into the vessel to control the temperature. The microwave was operated at 100% of 400 W for 2 h at 100 °C. Once complete, the vessel was naturally cooled to room temperature. A mixture with the ratio of 60/40 ethanol/dichloromethane was added, and then the solution was centrifuged to separate the crystals from the solution. Finally, the crystals were washed twice using ethanol before drying in an oven at 80 °C.

2.1. Characterization Methods. The structure of CC3 before and after being subjected to hydrate formation and dissociation was characterized using powder X-ray diffraction (XRD), field emission scanning electron microscope (FESEM), argon adsorption isotherm, and methane adsorption isotherm. The XRD used was a Siemens Kristalloflex 810 diffractometer that operated at a wavelength of 1.54059 Å, a voltage of 30 kV, and a current of 25 mA. The FESEM used was a JEOL JSM-7000F. The argon adsorption isotherms at 87 K and methane adsorption isotherm at 0 °C were collected using an ASAP 2020 porosimeter (Micromeritics, Norcross, GA), with the samples undergoing a degassing step at 200 °C for 8 h under vacuum. Surface areas were calculated using the cross-sectional diameter of Ar (0.142 nm) and the Brunauer–Emmett–Teller (BET) method, following the criteria described elsewhere.[73] The water adsorption isotherm was collected at 22 °C using an ASAP 2020 equipped with a vapor adsorption accessory. Prior to analysis, doubly distilled deionized water was loaded in the vapor flask, purged with nitrogen, and allowed to equilibrate at 22 °C for 8 h.

2.2. Scherrer Crystallite Size Calculations. To determine the size of the CC3 crystallites, the measured width of the peaks in the powder X-ray diffraction pattern was used in Scherrer's equation

$$L = \frac{K\lambda}{B\cos(\theta)} \tag{1}$$

where "L" represents the size of the crystallites, "K" is Scherrer's shape factor constant, "λ" is the wavelength, "B" is the full width of the peak at half its maximum intensity (FWHM), and "θ" is the diffraction angle.[74]

2.3. High-Pressure Differential Scanning Calorimeter Procedure. Hydrate formation and dissociation were observed using a high-pressure differential scanning calorimeter (HP-DSC) (VIIa Seteram Inc.) that has a resolution of 0.04 μW. The HP-DSC can operate between −45 to 120 °C and 0.1 to 15.4 MPa, with the precision of ±0.2 °C and ±25 kPa, respectively. The HP-DSC schematic is illustrated in Figure S1.

The procedures implemented in this study are parallel to our previous work.[52] To prepare the samples, first, deionized water was added to the HP-DSC cell. Next, the synthesized CC3 was added to the cell to achieve a specific water-to-CC3 mass ratio (R_w). Once the cell was placed in the HP-DSC, the system was pressurized with methane gas (Matherson, 99%).

The first method employed was a scan. The system was raised to a temperature of 30 °C at a heating rate of 0.5 °C/min and then held at 30 °C for 3 h. Next, the system was cooled to −30 °C at a rate of 0.3 °C/min and then heated to 30 °C at the same rate. This scan was repeated 3 times for each sample for the purpose of reproducibility of the results and to determine if the structural integrity of CC3 was maintained.

The second method was an isothermal test. Similar to the scanning method, the system was heated to 30 °C at a rate of 0.5 °C/min and then held at that temperature for 3 h. Then, the system was cooled at a rate of 0.8 °C/min to −10 °C. The temperature was held at −10 °C for 12 h before heating the system at a rate of 0.3 °C/min to 30 °C. This process was repeated 3 times.

The warming and cooling HP-DSC heat flux profiles result in exothermic peaks (formation) and endothermic peaks (dissociation). The dissociation temperature denotes the temperature at the onset of the dissociation peak. The area under the peak relates to how much ice or hydrate formed and dissociated in the HP-DSC system.

2.4. Water-to-Hydrate Conversion Calculations. The heat flux measurements of the endothermic hydrate dissociation peak obtained from the HP-DSC, denoted as H_{diss}, was used in the following equation to calculate how much water was converted into hydrate during the experiment.[75]

$$\text{hydrate conversion (\%)} = 100 \times \frac{H_{diss} MW_{H_2O} n_{HYD}}{H_{HYD}} \tag{2}$$

The other variables in the equation are as follows: molecular weight of water (MW_{H_2O} = 18 g/mol.); hydration number (n_{HYD} = 5.9),[75] and the heat of dissociation of the methane structure I hydrate (H_{HYD} = 54.4 kJ/mol.).[76]

3. RESULTS AND DISCUSSION

3.1. Impact of CC3 on Water-to-Hydrate Conversion. The addition of CC3 to the water and methane system in the high-pressure differential scanning calorimeter (HP-DSC) resulted in a significant increase in the water-to-hydrate conversion, as shown in Table 1.

The warming profiles gathered from the HP-DSC for selected experiments are shown in Figure 2. Full cooling and warming profiles are shown in Figure S2.

Without CC3, only 4.5% of the water converted to hydrates, whereas adding CC3 increased the water-to-hydrate conversion to as high as 87.5%. This improvement in conversion correlated directly with a rise in the amount of methane stored relative to the amount of water in the system, going from 0.42 mmol/g without CC3 to as high as 8.1 mmol/g with CC3.

The water-to-CC3 mass ratio (R_w) was varied to learn if the conversion or dissociation temperature was directly influenced by the concentration of CC3 in the system. Other studies using hollow silica,[77] HKUST-1,[52] activated carbon,[43] and nano silica suspension[78] as hydrate growth promoters found that the concentration of the promoter played a major role in the overall conversion results. Our previous study on HKUST-1 (copper-based metal organic framework) resulted in a direct

https://doi.org/10.1021/acs.jpcc.1c04657
J. Phys. Chem. C 2021, 125, 20512−20521

Table 1. Results of Scanning HP-DSC Experiments for a System with and without CC3, Displaying Water-to-Hydrate Conversion, Hydrate Dissociation Temperature, and the Amount of Methane Stored Relative to the Amount of Water in the System[a]

R_w: ratio of H_2O to CC3 (g/g)	water to hydrate conversion (%)	dissociation temperature (°C)	CH_4 stored to H_2O in system (mmol/g)
No CC3	4.5	11.5	0.42
0.47	82.2	10.2	7.6
0.65	85.3	9.9	7.9
0.86	86.9	9.9	8.0
0.93	80.1	10.3	8.1
1.22	87.5	10.2	8.1
1.81	68.0	10.7	6.3
3.98	10.7	11.2	1.0
6.02	10.2	11.1	1.0
6.20	9.8	11.3	0.9

[a]Values correspond to the third cycle of hydrate formation and dissociation.

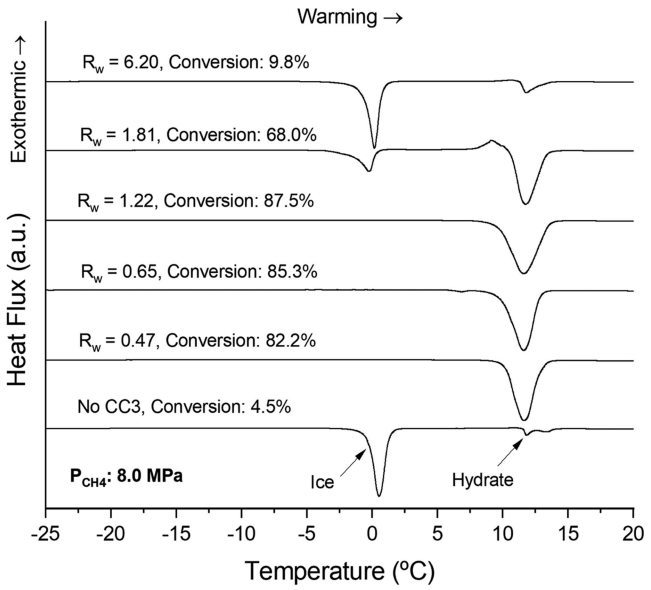

Figure 2. HP-DSC warming profiles for selected water-to-CC3 mass ratio and for a system without CC3, where the endothermic peaks represent dissociation of hydrate or ice, and the onset of the peaks corresponds to the dissociation temperature.

correlation between conversion and R_w; 20.5% conversion at R_w of 0.39 increased to 87.2% conversion at R_w of 1.08.[52] For CC3, from the R_w of 0.47 to 1.22, the average water-to-hydrate conversion was 84.2 ± 2.9% without any ice formation on the third cycle of hydrate formation. In contrast, in the first and second cycles, ice formation was observed. When the R_w reached 1.81, only 68.0% of the water converted to hydrates, and ice formed on the third cycle. Therefore, the optimal R_w was 1.22. The water-to-hydrate conversion continued to decline as the R_w increased, and by R_w of 6.20, the conversion dropped to only 9.8%. Although this conversion is low compared to the other ratios, it is more than double the amount in a system without any CC3. The doubled conversion indicates that the large surface area of the synthesized CC3 (415.6 m^2/g) played a key role in promoting growth, as the crystals still increase the gas-to-water contact area as compared to bulk water.

Another property of CC3 that influences the water-to-hydrate conversion is the high methane adsorption capacity of CC3. Methane adsorption isotherms conducted at a low pressure of 1.2 bar and at 273 K, shown in Figure S3, revealed that the synthesized CC3 used in this study adsorbed 1.60 mmol/g. Studies on methane hydrate formation in the presence of porous materials (excluding POCs) with high methane adsorption have found that the adsorbed methane can form gas bubbles or a gas layer on the surface of the material.[79,80] In these studies, methane bubbles or layers acted as nucleation sites and prevented the surface of the material from negatively interfering with the water ordering.[79,81,82] It is believed that the methane adsorbed on the structure of CC3 may result in a similar effect. Competitive water/methane adsorption occurs on the synthesized CC3, as the amount of water adsorbed is 3.67 mmol/g versus 1.60 mmol/g of methane. (See Figure S4 for the water isotherm). Note, the water adsorbed on this synthesized CC3 is one-third of that found in a study in the literature on CC3, which corresponds to the synthesized CC3 in this work having one-third of the surface area of the CC3 in that study.[83] A study on the effects of hydrophobicity of porous materials on methane hydrate growth indicated that although a flat hydrophobic surface promotes hydrate growth more than a hydrophilic one, the optimal internal surface of a pore large enough to contain hydrates is one with moderate wettability.[80] Therefore, the wettability of the synthesized CC3 combined with the competitive water/methane adsorption may provide a relatively good balance between promoting hydrate formation in both confined spaces and on the external surface of the crystal. This adsorbed methane may also account for the conversion at high water-to-CC3 mass ratios being twice that of a system without CC3, as the adsorbed methane creates a gas-to-water interface at the surface of CC3.

3.2. Impact of CC3 on Hydrate Dissociation Temperature. The addition of CC3 resulted in a decrease of hydrate dissociation temperature on average by 1.4 ± 0.1 °C for the water-to-CC3 mass ratios of 0.47−1.22. A shift of the hydrate dissociation temperature to lower values is indicative of a reduction in the stability of the hydrate structure.[40,84]

A change in hydrate stability (i.e., thermodynamic phase envelope) has been directly correlated to hydrates that formed in confined spaces, such as interstitial spacing caused by uneven crystallite packing discussed later, as the constricted space leads to lower water activity, and thus less stable hydrates.[58,85,86] A study on the metal organic framework MIL-53 as a hydrate growth promoter found that the hydrates confined in the pores of the material exhibited inhibited thermodynamic behavior (i.e., hydrate destabilization), resulting in hydrates dissociating at lower temperatures, attributing the decrease to reduced water activity.[49] Another study using porous silica glass observed that the hydrate dissociation temperature decreased with decreasing pore diameter, which shows that the extent of thermodynamic effects depends upon the type of material used.[39] A study on methane hydrate growth in silica gels reported a shift in hydrate dissociation temperature as large as 6 °C and found that the confinement effect on dissociation temperature tapered off for materials with pore sizes larger than 100 nm.[48] For certain materials, there is an optimum pore size that results in the highest methane storage capacity, such as with model carbon at a pore

https://doi.org/10.1021/acs.jpcc.1c04657
J. Phys. Chem. C 2021, 125, 20512−20521

size of 25 nm, despite the fact that it exhibited a depressed dissociation temperature due to constricted water activity in the pores.[87] Additionally, the chemical composition of the material can alter the stabilization of the hydrates inside of the pores, such as how a very hydrophilic pore inhibits formation.[80] All of these factors must be taken into consideration when evaluating confined hydrate growth.

Cryogenic argon isotherms (87 K), shown in Figure 3, were used in place of typical nitrogen isotherms (77 K) to measure the pore size distribution of CC3, as the kinetic diameter of argon (3.4 Å) is small enough to probe the limiting aperture (3.6 Å) of CC3.

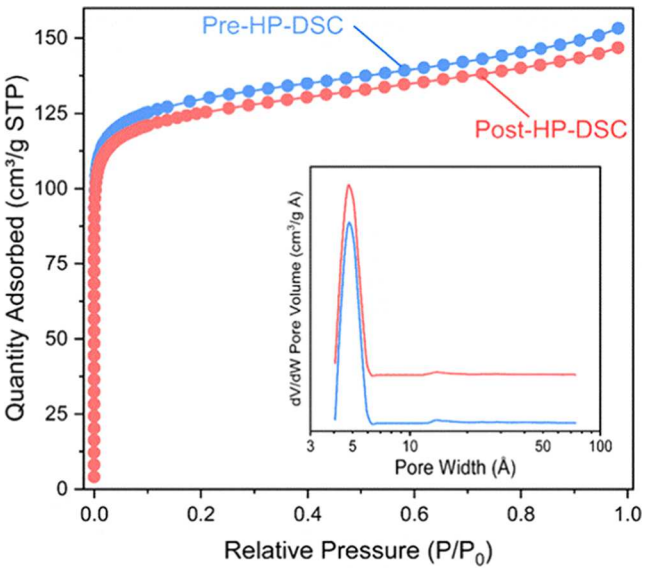

Figure 3. Argon isotherms conducted at 87 K, with insets displaying the pore size distributions calculated from NLDFT for CC3 samples before and after exposure to 3 cycles of hydrate formation and dissociation.

Our results indicate that the synthesized CC3 had a primary cavity size (intrinsic pore diameter) of 5 Å, in agreement with the calculated cavity size reported in the literature.[88] Hydrates cannot form inside of the CC3 cavity, as the typical methane hydrate structure I has a unit cell size of 12 Å.[10,12] The more likely location of confined hydrate formation is in the void spaces caused by uneven packing of CC3 cages or by some incomplete cages, as illustrated in Figure 4a.[89]

These void spaces would account for the secondary pore size at approximately 15 Å observed in the argon isotherms at 87 K, which represents approximately 5% of the total pore volume. Seminal work by Cooper et al. also observed the presence of larger pore sizes in the range of 12−15 Å, which can accommodate the hydrate structure I unit cell.[13]

The other type of confined space that could contain a methane hydrate is the interstitial spacing between the assembled CC3 crystallites, exemplified in Figure 4b. These crystallites pack together to form polycrystalline particles in an octahedron shape, illustrated in Figure 4c, which results in the overall external surface of the crystal, where more hydrate formation can take place.

At the higher water-to-CC3 mass ratio of 3.98, the drop in conversion to 10.7% still exhibited a depressed dissociation temperature (11.1 °C) relative to a system without CC3 (11.5 °C). The decrease suggests that in the void and interstitial spaces, adsorbed methane promotes hydrate growth in these confined spaces despite the excess amount of water in the system.

3.3. CC3 Influences Hydrate Nucleation Induction Time. Addition of CC3 to the HP-DSC greatly influenced the kinetics of hydrate formation in two ways: (1) reduced the hydrate nucleation induction time and (2) promoted consistent hydrate formation. The isothermal HP-DSC experiments conducted at −10 °C, as shown in Figure S5, resulted in the hydrate nucleation induction time in a system without CC3 forming hydrates in only two out of the six experiments, with times 2.0 and 9.7 h, with four out of six cycles not forming hydrates at all. The varying induction times are a result of the stochastic nature of hydrate formation, another barrier to commercializing hydrates for natural gas storage and transportation.[82] The isothermal experiments with CC3 showed improved results, as it produced hydrates for all four cycles conducted, as shown in Figure S5, with a consistent induction time of 0.8 ± 0.1 h.

The properties of CC3 that influenced the improved kinetics of hydrate formation are its high methane adsorption capacity and reversible water uptake of CC3.[62,83] As mentioned previously, adsorbed methane acts as a source for hydrate growth, thus promoting growth in the void and interstitial spaces. As for water adsorption, a study on a microporous

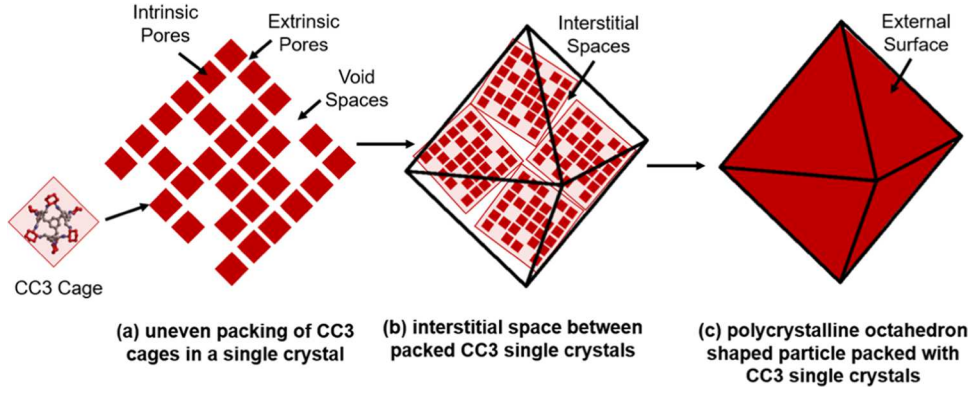

Figure 4. Illustration of the stages of CC3 particle packing: (a) uneven packing of CC3 cages in a single crystal creating void spaces ~1.2 to 1.5 nm, (b) assembled CC3 single crystals with diameter ~25 to 50 nm forming interstitial spacing, and (c) octahedron polycrystalline particles at ~2 μm in diameter provide an external surface for gas hydrate growth.

https://doi.org/10.1021/acs.jpcc.1c04657
J. Phys. Chem. C 2021, 125, 20512−20521

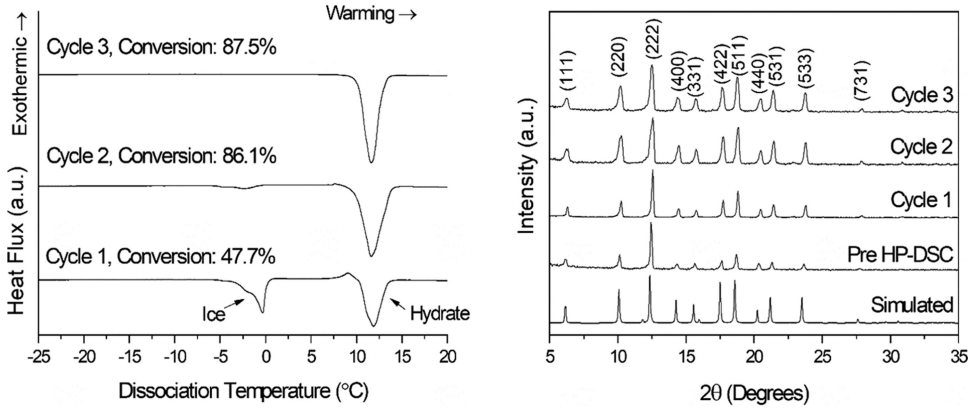

Figure 5. (left) HP-DSC warming profiles for CC3 over the course of 3 consecutive hydrate formation and dissociation cycles; (right) XRD patterns of simulated αCC3, sample before hydrate formation and dissociation and after 3 consecutive cycles.

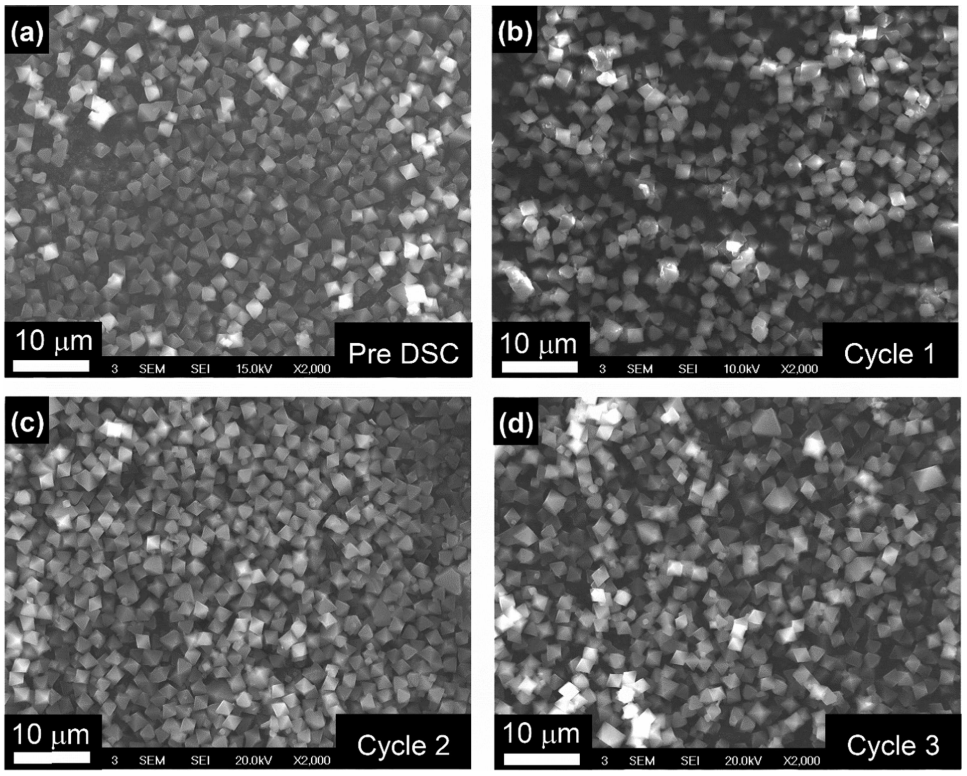

Figure 6. SEM images of the synthesized CC3 (a) before hydrate formation and dissociation in the HP-DSC, (b) after 1 cycle of hydrate formation and dissociation, (c) after 2 cycles, and (d) after 3 cycles.

RHO zeolite as a hydrate promoter found that the hydrated micropores acted as hydrate nucleation sites.[55] The water uptake in CC3 results in hydrated micropores, as one CC3 cage can adsorb up to 12 water molecules, and reversible binding allows the water to disengage from the adsorption sites to participate in hydrate formation.[83] Therefore, the synergistic properties of water and methane adsorption lead to the exceptional performance of CC3 as a kinetic hydrate promoter.

3.4. Recyclability of CC3 after Hydrate Formation and Dissociation. Multiple cycles of hydrate formation and dissociation were conducted with CC3 in the HP-DSC to determine if the performance of CC3 was repeatable. The results showed interesting behavior. The water-to-hydrate conversion after the first cycle was on average 30% lower than that of the second cycle for R_w of 0.47−1.22. For the same range of R_w, ice formation took place during the first cycle, yet no ice formed during the second nor during the third cycle, as exemplified for R_w of 1.22 shown in Figure 5.

For the CC3 sample subjected to 5 cycles of hydrate formation and dissociation, the second, third, fourth, and fifth cycles only deviated by ±0.2%, suggesting that any changes to the CC3 structure stops after the first cycle.

The powder XRD patterns, shown in Figure 5, exhibited a similar trend to the conversion: the peak widths and relative intensities change from the first cycle to the second and then stayed consistent between the second and third cycle. Despite the change, all of the patterns match the simulated αCC3 XRD pattern well, indicating the robust structural stability of CC3. To further investigate why the change occurred, the measured peak width at half of the maximum intensity of the peak was used to calculate the average Scherrer crystallite size (i.e., single crystal size) for all of the peaks using Scherrer's equation

https://doi.org/10.1021/acs.jpcc.1c04657
J. Phys. Chem. C 2021, 125, 20512−20521

shown in the experimental methods. The Scherrer crystallite size pre HP-DSC was 48.3 ± 7 nm, then it dropped slightly to 44.2 ± 5 nm after the first cycle, then drastically dropped to 27.6 ± 5 and 26.2 ± 5 nm for the second and third cycle, respectively. The similar Scherrer crystallite size of the pre HP-DSC and the post first cycle samples suggest that the amount of time exposed to the HP-DSC is what decreases the Scherrer crystallite size. To determine the effects of time on CC3, the HP-DSC isothermal 12 h experiments were conducted. After the first cycle, the conversion reached 88.2%, and the powder XRD pattern revealed that the Scherrer crystallite size after the isothermal test was 27.3 ± 5 nm. Therefore, the 39% decrease in Scherrer crystallite size was most likely caused by the amount of time exposed to the HP-DSC. The smaller Scherrer crystallite size would lead to more interstitial spacing in the polycrystalline particle, resulting in enhanced water-to-hydrate conversion. Notably, the overall pore volume for the ∼12 to 15 Å pores decreased by ∼3%, indicating that as the crystallites change size, some of the void spaces are lost at the expense of larger interstitial spacing formation. Furthermore, the relative peak intensity ratios for some of the CC3 planes show a similar trend to the crystallite size decrease. For the (222)/(400) peak ratios, the pre HP-DSC sample is 5.7; then, it drops to 4.7 after the first cycle and 2.71 and 3.22 after the second and third cycles, respectively. The change in peak intensity ratios is indicative of specific planes of the crystals exhibiting preferential exposure.[90,91] This observation could be attributed to the change in Scherrer crystallite size, as the decrease in size may also alter the crystallites' orientation.

The time length effect on the conversion in the presence of CC3 also may be influenced by the diffusion of methane and water into the structure. A study on the diffusion of methane and carbon dioxide through CC3 using a zero-length column discovered that methane diffuses faster than carbfon dioxide due to methane's tetrahedral shape passing through the pore pathways better than the linear shape of carbon dioxide, despite the kinetic diameter of methane (3.8 Å) being larger than carbon dioxide (3.3 Å).[66] When a mixture of 10:90 molar ratio of carbon dioxide to methane was flowed through CC3, the diffusion rate of methane and carbon dioxide decreased due to the competitive adsorption between the two.[69] A similar competitive adsorption effect may be restricting the flow of methane and water through the structure, as the shape of water is bent, and both molecules adsorb well to CC3. Slow diffusion would require more time for the competing methane and water to diffuse through the pores to ideal hydrate nucleation sites and promote more water-to-hydrate conversion.

Representative SEM images of the synthesized CC3 sample before and after 3 cycles of hydrate formation and dissociation are shown in Figure 6.

For CC3, no morphological changes occurred. The particle size stayed consistently at 1.9 ± 0.2, 1.8 ± 0.1, 1.9 ± 0.2, and 1.9 ± 0.4 μm for the pre HP-DSC and post HP-DSC for the first, second, and third cycle, respectively. Overall, CC3 maintained its crystallinity and morphology well, indicating it is a highly recyclable hydrate promoter.

This work on CC3 uses similar experimental conditions as our previous studies on metal organic frameworks HKUST-1[52] and ZIFs.[92] While CC3, HKUST-1, and ZIFs exhibited similar water-to-hydrate conversion, CC3 decreased the hydrate induction time to a greater extent as compared to HKUST-1 and ZIFs. Furthermore, the advantage of CC3 over HKUST-1 and ZIFs is related to its more robust life cycle. Specifically, CC3 has improved water stability and has a longer life cycle as a promoter as compared to HKUST-1 and ZIFs.

4. CONCLUSIONS

In summary, we demonstrate that a prototypical porous organic cage, denoted as CC3, acts as an efficient growth promoter for methane hydrate formation. Specifically, the addition of CC3 to the HP-DSC water and methane system results in a significant rise in water-to-hydrate conversion from 4.5 ± 0.4% without CC3 to a high of 87.5 ± 1.0% with CC3 (for the second and third cycles). The increase in hydrate growth results from CC3's high methane adsorption capacity and large surface area. The presence of CC3 induced a reduction in the hydrate dissociation temperature, going from 11.5 ± 0.1 °C without CC3 to as low as 9.9 ± 0.5 °C with CC3. This reduction suggests that hydrate formation took place in a confined space. Argon isotherms at 87 K determined that the intrinsic pore size is 5 Å and secondary pore size at approximately 15 Å, representing ∼5% of the total pores. The secondary pore corresponds to void spaces in the cage packing, a size which can encompass a methane hydrate unit cell, 12 Å. Hydrate formation also induced a decrease in CC3 crystallite size from 48.3 to 26.2 nm, which provided more interstitial spacing and thus increased the hydrate conversion after the first cycle of hydrate formation and dissociation. Addition of CC3 resulted in consistent hydrate formation in 0.8 ± 0.1 h, whereas a system without CC3 only formed hydrates two out of six times. The likely reasons for the consistency are the synergistic effects of the high methane adsorbed (source of methane for hydrate formation) and the reversible water uptake (water in pores acts as hydrate nucleation site). The remarkably enhanced performance of CC3 as a methane hydrate growth promoter and its robust structural integrity make it a highly appealing material for effective methane storage in gas hydrates.

■ ASSOCIATED CONTENT

Supporting Information

The Supporting Information is available free of charge at https://pubs.acs.org/doi/10.1021/acs.jpcc.1c04657.

Supporting information includes a schematic of the HP-DSC, full cooling and warming HP-DSC profiles, methane adsorption isotherm, and HP-DSC isothermal profiles (PDF)

■ AUTHOR INFORMATION

Corresponding Authors

Moises A. Carreon − *Chemical and Biological Engineering Department, Colorado School of Mines, Golden, Colorado 80401, United States;* orcid.org/0000-0001-6391-2478; Email: mcarreon@mines.edu

Carolyn A. Koh − *Chemical and Biological Engineering Department, Colorado School of Mines, Golden, Colorado 80401, United States;* orcid.org/0000-0003-3452-4032; Email: ckoh@mines.edu

Authors

Shurraya Denning − *Chemical and Biological Engineering Department, Colorado School of Mines, Golden, Colorado 80401, United States*

Jolie M. Lucero − *Chemical and Biological Engineering Department, Colorado School of Mines, Golden, Colorado 80401, United States;* orcid.org/0000-0002-4606-7118
Ahmad A. A. Majid − *Chemical and Biological Engineering Department, Colorado School of Mines, Golden, Colorado 80401, United States*
James M. Crawford − *Chemical and Biological Engineering Department, Colorado School of Mines, Golden, Colorado 80401, United States;* orcid.org/0000-0003-3614-6055

Complete contact information is available at: https://pubs.acs.org/10.1021/acs.jpcc.1c04657

Notes

The authors declare no competing financial interest.

■ ACKNOWLEDGMENTS

Financial support from the National Science Foundation (CBET award # 1835924) is gratefully acknowledged.

■ REFERENCES

(1) Huang, K.; Miller, J. B.; Huber, G. W.; Dumesic, J. A.; Maravelias, C. T. A General Framework for the Evaluation of Direct Nonoxidative Methane Conversion Strategies. *Joule* **2018**, *2*, 349−365.
(2) Chong, Z. R.; Yang, S. H. B.; Babu, P.; Linga, P.; Li, X. Sen. Review of Natural Gas Hydrates as an Energy Resource: Prospects and Challenges. *Appl. Energy* **2016**, *162*, 1633−1652.
(3) Majid, A. A. A.; Koh, C. A. Self-Preservation Phenomenon in Gas Hydrates and Its Application for Energy Storage. In *Intra- and Intermolecular Interactions Between Non-covalently Bonded Species*; Elsevier, 2021; pp 267−285.
(4) Gudmundson, J.; Borrehaug, A. Natural Gas Hydrate - an Alternative to Liquefied Natural Gas? *Pet. Rev.* **1996**, 232−235.
(5) Dooner, M.; Wang, J. Compressed-Air Energy Storage. In *Future Energy: Improved, Sustainable and Clean Options for Our Planet*; Elsevier, 2020; pp 279−312.
(6) Wang, W.; Bray, C. L.; Adams, D. J.; Cooper, A. I. Methane Storage in Dry Water Gas Hydrates. *J. Am. Chem. Soc.* **2008**, *130*, 11608−11609.
(7) Stern, L. A.; Circone, S.; Kirby, S. H.; Durham, W. B. Anomalous Preservation of Pure Methane Hydrate at 1 Atm. *J. Phys. Chem. B* **2001**, *105*, 1756−1762.
(8) Hao, W.; Wang, J.; Fan, S.; Hao, W. *Evaluation and Analysis Method for Natural Gas Hydrate Storage and Transportation Processes* **2008**, *49*, 2546−2553.
(9) Veluswamy, H. P.; Kumar, A.; Seo, Y.; Lee, J. D.; Linga, P. A Review of Solidified Natural Gas (SNG) Technology for Gas Storage via Clathrate Hydrates. *Appl. Energy* **2018**, *216*, 262−285.
(10) Sloan, E. D.; Koh, C. A. *Clathrate Hydrates of Natural Gases*, 3rd ed.; CRC Press: New York, 2008.
(11) Methane/Propane Double Hydrate Janda Lab, https://ps.uci.edu/group/kcjanda/research/methanepropane-double-hydrate. (accessed May 18, 2020).
(12) Chen, L.; Reiss, P. S.; Chong, S. Y.; Holden, D.; Jelfs, K. E.; Hasell, T.; Little, M. A.; Kewley, A.; Briggs, M. E.; Stephenson, A.; et al. Separation of Rare Gases and Chiral Molecules by Selective Binding in Porous Organic Cages. *Nat. Mater.* **2014**, *13*, 954−960.
(13) Tozawa, T.; Jones, J. T. A.; Swamy, S. I.; Jiang, S.; Adams, D. J.; Shakespeare, S.; Clowes, R.; Bradshaw, D.; Hasell, T.; Chong, S. Y.; et al. Porous Organic Cages. *Nat. Mater.* **2009**, *8*, 973−978.
(14) Gudmundsson, J. S.; Parlaktuna, M.; Khokhar, A. A. Storing Natural Gas as Frozen Hydrate. *SPE Prod. Facil.* **1994**, *9*, 69−73.
(15) Koh, C. A.; Sloan, E. D. Natural Gas Hydrates: Recent Advances and Challenges in Energy and Environmental Applications. *AIChE J.* **2007**, *53*, 1636−1643.
(16) Zhong, J. R.; Zeng, X. Y.; Zhou, F. H.; Ran, Q. D.; Sun, C. Y.; Zhong, R. Q.; Yang, L. Y.; Chen, G. J.; Koh, C. A. Self-Preservation and Structural Transition of Gas Hydrates during Dissociation below the Ice Point: An in Situ Study Using Raman Spectroscopy. *Sci. Rep.* **2016**, *6*, No. 38855.
(17) Gudmundsson, J.; Borrehaug, A. Frozen Hydrate for Transport of Natural Gas. In *Frozen Hydrate for Transport of Natural Gas*; Toulouse, 1996; pp 415−422.
(18) Mimachi, H.; Takahashi, M.; Takeya, S.; Gotoh, Y.; Yoneyama, A.; Hyodo, K.; Takeda, T.; Murayama, T. Effect of Long-Term Storage and Thermal History on the Gas Content of Natural Gas Hydrate Pellets under Ambient Pressure. *Energy Fuels* **2015**, *29*, 4827−4834.
(19) Bhattacharjee, G.; Veluswamy, H. P.; Kumar, A.; Linga, P. Stability Analysis of Methane Hydrates for Gas Storage Application. *Chem. Eng. J.* **2021**, *415*, No. 128927.
(20) Giavarini, C.; MacCioni, F.; Santarelli, M. L. Dissociation Rate of THF-Methane Hydrates. *Pet. Sci. Technol.* **2008**, *26*, 2147−2158.
(21) Zhang, J. S.; Lee, S.; Lee, J. W. Kinetics of Methane Hydrate Formation from SDS Solution. *Ind. Eng. Chem. Res.* **2007**, *46*, 6353−6359.
(22) Shi, L.; Shen, X.; Ding, J.; Liang, D. Experimental Study on the Formation Kinetics of Methane Hydrates in the Presence of Tetrabutylammonium Bromide. *Energy Fuels* **2017**, *31*, 8540−8547.
(23) Shi, L.; Liang, D. Semiclathrate Hydrate Phase Behaviour and Structure for CH4 in the Presence of Tetrabutylammonium Fluoride (TBAF). *J. Chem. Thermodyn* **2019**, *135*, 252−259.
(24) Lv, Q.-N.; Li, X.; Chen, Z. Y.; Feng, J. C. Phase Equilibrium and Dissociation Enthalpies for Hydrates of Various Water-Insoluble Organic Promoters with Methane. *J. Chem. Eng. Data* **2013**, *58*, 3249−3253.
(25) Bhattacharjee, G.; Goh, M. N.; Arumuganainar, S. E. K.; Zhang, Y.; Linga, P. Ultra-Rapid Uptake and the Highly Stable Storage of Methane as Combustible Ice †. *Energy Environ. Sci.* **2020**, *13*, 4946.
(26) Baek, S.; Ahn, Y. H.; Zhang, J.; Min, J.; Lee, H.; Lee, J. W. Enhanced Methane Hydrate Formation with Cyclopentane Hydrate Seeds. *Appl. Energy* **2017**, *202*, 32−41.
(27) Bhattacharjee, G.; Veluswamy, H. P.; Kumar, R.; Linga, P. Seawater Based Mixed Methane-THF Hydrate Formation at Ambient Temperature Conditions. *Appl. Energy* **2020**, *271*, No. 115158.
(28) Inkong, K.; Veluswamy, H. P.; Rangsunvigit, P.; Kulprathipanja, S.; Linga, P. Investigation on the Kinetics of Methane Hydrate Formation in the Presence of Methyl Ester Sulfonate. *J. Nat. Gas Sci. Eng.* **2019**, *71*, No. 102999.
(29) Veluswamy, H. P.; Kumar, A.; Kumar, R.; Linga, P. An Innovative Approach to Enhance Methane Hydrate Formation Kinetics with Leucine for Energy Storage Application. *Appl. Energy* **2017**, *188*, 190−199.
(30) Veluswamy, H. P.; Lee, P. Y.; Premasinghe, K.; Linga, P. Effect of Biofriendly Amino Acids on the Kinetics of Methane Hydrate Formation and Dissociation. *Ind. Eng. Chem. Res.* **2017**, *56*, 6145−6154.
(31) Shi, C.; Chai, F.; Yang, M.; Song, Y.; Wang, F.; Zhou, H.; Ling, Z. Enhance Methane Hydrate Formation Using Fungus Confining Sodium Dodecyl Sulfate Solutions for Methane Storage. *J. Mol. Liq.* **2021**, *333*, No. 116020.
(32) Lin, Y.; Veluswamy, H. P.; Linga, P. Effect of Eco-Friendly Cyclodextrin on the Kinetics of Mixed Methane-Tetrahydrofuran Hydrate Formation. *Ind. Eng. Chem. Res.* **2018**, *57*, 5944−5950.
(33) Inkong, K.; Rangsunvigit, P.; Kulprathipanja, S.; Linga, P. Effects of Temperature and Pressure on the Methane Hydrate Formation with the Presence of Tetrahydrofuran (THF) as a Promoter in an Unstirred Tank Reactor. *Fuel* **2019**, *255*, No. 115705.
(34) Hao, W.; Wang, J.; Fan, S.; Hao, W. Study on Methane Hydration Process in a Semi-Continuous Stirred Tank Reactor. *Energy Convers. Manag.* **2007**, *48*, 954−960.
(35) Luo, Y.-T.; Zhu, J. H.; Fan, S. S.; Chen, G. J. Study on the Kinetics of Hydrate Formation in a Bubble Column. *Chem. Eng. Sci.* **2007**, *62*, 1000−1009.

(36) Filarsky, F.; Schmuck, C.; Schultz, H. J. Impact of Modified Silica Beads on Methane Hydrate Formation in a Fixed-Bed Reactor. *Ind. Eng. Chem. Res.* **2019**, *58*, 16687−16695.
(37) Lee, J.; Shin, C.; Lee, Y. Experimental Investigation to Improve the Storage Potentials of Gas Hydrate under the Unstirring Condition. *Energy Fuels* **2010**, *24*, 1129−1134.
(38) Inkong, K.; Veluswamy, H. P.; Rangsunvigit, P.; Kulprathipanja, S.; Linga, P. Innovative Approach to Enhance the Methane Hydrate Formation at Near-Ambient Temperature and Moderate Pressure for Gas Storage Applications. *Ind. Eng. Chem. Res.* **2019**, *58*, 22178−22192.
(39) Smith, D. H.; Wilder, J. W.; Seshadri, K. Methane Hydrate Equilibria in Silica Gels with Broad Pore-Size Distributions. *AIChE J.* **2002**, *48*, 393−400.
(40) Chong, Z. R.; Yang, M.; Khoo, B. C.; Linga, P. Size Effect of Porous Media on Methane Hydrate Formation and Dissociation in an Excess Gas Environment. *Ind. Eng. Chem. Res.* **2016**, *55*, 7981−7991.
(41) Pasieka, J.; Coulombe, S.; Servio, P. Investigating the Effects of Hydrophobic and Hydrophilic Multi-Wall Carbon Nanotubes on Methane Hydrate Growth Kinetics. *Chem. Eng. Sci.* **2013**, *104*, 998−1002.
(42) Cuadrado-Collados, C.; Fauth, F.; Such-Basañez, I.; Martínez-Escandell, M.; Silvestre-Albero, J. Methane Hydrate Formation in the Confined Nanospace of Activated Carbons in Seawater Environment. *Microporous Mesoporous Mater.* **2018**, *255*, 220−225.
(43) Cuadrado-Collados, C.; Majid, A. A. A.; Martínez-Escandell, M.; Daemen, L. L.; Missyul, A.; Koh, C.; Silvestre-Albero, J. Freezing/Melting of Water in the Confined Nanospace of Carbon Materials: Effect of an External Stimulus. *Carbon* **2020**, *158*, 346−355.
(44) Cuadrado-Collados, C.; Farrando-Pérez, J.; Martínez-Escandell, M.; Missyul, A.; Silvestre-Albero, J. Effect of Additives in the Nucleation and Growth of Methane Hydrates Confined in a High-Surface Area Activated Carbon Material. *Chem. Eng. J.* **2020**, *388*, No. 124224.
(45) Babu, P.; Kumar, R.; Linga, P. A New Porous Material to Enhance the Kinetics of Clathrate Process: Application to Precombustion Carbon Dioxide Capture. *Environ. Sci. Technol.* **2013**, *47*, 13191−13198.
(46) Casco, M. E.; Rey, F.; Jordá, J. L.; Rudić, S.; Fauth, F.; Martínez-Escandell, M.; Rodríguez-Reinoso, F.; Ramos-Fernández, E. V.; Silvestre-Albero, J. Paving the Way for Methane Hydrate Formation on Metal-Organic Frameworks (MOFs). *Chem. Sci.* **2016**, *7*, 3658−3666.
(47) Mu, L.; Liu, B.; Liu, H.; Yang, Y.; Sun, C.; Chen, G. A Novel Method to Improve the Gas Storage Capacity of ZIF-8. *J. Mater. Chem.* **2012**, *22*, 12246−12252.
(48) Liu, H.; Zhan, S.; Guo, P.; Fan, S.; Zhang, S. Understanding the Characteristic of Methane Hydrate Equilibrium in Materials and Its Potential Application. *Chem. Eng. J.* **2018**, *349*, 775−781.
(49) Kim, D.; Ahn, Y. H.; Lee, H. Phase Equilibria of CO2 and CH4 Hydrates in Intergranular Meso/Macro Pores of MIL-53 Metal Organic Framework. *J. Chem. Eng. Data* **2015**, *60*, 2178−2185.
(50) He, Z.; Zhang, K.; Jiang, J. Formation of CH4 Hydrate in a Mesoporous Metal-Organic Framework MIL-101: Mechanistic Insights from Microsecond Molecular Dynamics Simulations. *J. Phys. Chem. Lett.* **2019**, *10*, 7002−7008.
(51) Cuadrado-Collados, C.; Mouchaham, G.; Daemen, L.; Cheng, Y.; Ramirez-Cuesta, A.; Aggarwal, H.; Missyul, A.; Eddaoudi, M.; Belmabkhout, Y.; Silvestre-Albero, J. Quest for an Optimal Methane Hydrate Formation in the Pores of Hydrolytically Stable Metal-Organic Frameworks. *J. Am. Chem. Soc.* **2020**, *142*, 13391−13397.
(52) Denning, S.; Majid, A. A.; Lucero, J. M.; Crawford, J. M.; Carreon, M. A.; Koh, C. A. Metal−Organic Framework HKUST-1 Promotes Methane Hydrate Formation for Improved Gas Storage Capacity. *ACS Appl. Mater. Interfaces* **2020**, *12*, 53510−53518.
(53) Zang, X.; Du, J.; Liang, D.; Fan, S.; Tang, C. Influence of A-Type Zeolite on Methane Hydrate Formation. *Chinese J. Chem. Eng.* **2009**, *17*, 854−859.
(54) Zhao, Y.; Zhao, J.; Liang, W.; Gao, Q.; Yang, D. Semi-Clathrate Hydrate Process of Methane in Porous Media-Microporous Materials of 5A-Type Zeolites. *Fuel* **2018**, *220*, 185−191.
(55) Andres-Garcia, E.; Dikhtiarenko, A.; Fauth, F.; Silvestre-Albero, J.; Ramos-Fernández, E. V.; Gascon, J.; Corma, A.; Kapteijn, F. Methane Hydrates: Nucleation in Microporous Materials. *Chem. Eng. J.* **2019**, *360*, 569−576.
(56) Kim, N.-J.; Park, S.-S.; Shin, S.-W.; Hyun, J.-H.; Chun, W. An Experimental Investigation into the Effects of Zeolites on the Formation of Methane Hydrates. *Int. J. Energy Res.* **2015**, *39*, 26−32.
(57) Mohammed, S.; Asgar, H.; Deo, M.; Gadikota, G. Interfacial and Confinement-Mediated Organization of Gas Hydrates, Water, Organic Fluids, and Nanoparticles for the Utilization of Subsurface Energy and Geological Resources. *Energy Fuels* **2021**, *35*, 4687−4710.
(58) Borchardt, L.; Casco, M. E.; Silvestre-Albero, J. Methane Hydrate in Confined Spaces: An Alternative Storage System. *ChemPhysChem* **2018**, *19*, 1298−1314.
(59) Lucero, J. M.; Jasinski, J. B.; Song, M.; Li, D.; Liu, L.; Liu, J.; De Yoreo, J. J.; Thallapally, P. K.; Carreon, M. A. Synthesis of Porous Organic Cage CC3 via Solvent Modulated Evaporation. *Inorganica Chim. Acta* **2020**, *501*, No. 119312.
(60) Little, M. A.; Cooper, A. I. The Chemistry of Porous Organic Molecular Materials. *Adv. Funct. Mater.* **2020**, *30*, No. 1909842.
(61) Komulainen, S.; Roukala, J.; Zhivonitko, V. V.; Javed, M. A.; Chen, L.; Holden, D.; Hasell, T.; Cooper, A.; Lantto, P.; Telkki, V. V. Inside Information on Xenon Adsorption in Porous Organic Cages by NMR. *Chem. Sci.* **2017**, *8*, 5721−5727.
(62) Charles, C. D.; Bloch, E. D. High-Pressure Methane Storage and Selective Gas Adsorption in a Cyclohexane-Functionalised Porous Organic Cage. *Supramol. Chem.* **2019**, *31*, 508−513.
(63) Hasell, T.; Armstrong, J. A.; Jelfs, K. E.; Tay, F. H.; Thomas, K. M.; Kazarian, S. G.; Cooper, A. I. High-Pressure Carbon Dioxide Uptake for Porous Organic Cages: Comparison of Spectroscopic and Manometric Measurement Techniques. *Chem. Commun.* **2013**, *49*, 9410−9412.
(64) Liu, M.; Chen, L.; Lewis, S.; Chong, S. Y.; Little, M. A.; Hasell, T.; Aldous, I. M.; Brown, C. M.; Smith, M. W.; Morrison, C. A.; et al. Three-Dimensional Protonic Conductivity in Porous Organic Cage Solids. *Nat. Commun.* **2016**, *7*, No. 12750.
(65) Kewley, A.; Stephenson, A.; Chen, L.; Briggs, M. E.; Hasell, T.; Cooper, A. I. Porous Organic Cages for Gas Chromatography Separations. *Chem. Mater.* **2015**, *27*, 3207−3210.
(66) Sun, J. K.; Zhan, W. W.; Akita, T.; Xu, Q. Toward Homogenization of Heterogeneous Metal Nanoparticle Catalysts with Enhanced Catalytic Performance: Soluble Porous Organic Cage as a Stabilizer and Homogenizer. *J. Am. Chem. Soc.* **2015**, *137*, 7063−7066.
(67) Lucero, J. M.; Carreon, M. A. Separation of Light Gases from Xenon over Porous Organic Cage Membranes. *ACS Appl. Mater. Interfaces* **2020**, *12*, 32182−32188.
(68) Hasell, T.; Miklitz, M.; Stephenson, A.; Little, M. A.; Chong, S. Y.; Clowes, R.; Chen, L.; Holden, D.; Tribello, G. A.; Jelfs, K. E.; et al. Porous Organic Cages for Sulfur Hexafluoride Separation. *J. Am. Chem. Soc.* **2016**, *138*, 1653−1659.
(69) Gelles, T.; Rownaghi, A. A.; Rezaei, F. Diffusion Kinetics of CO2, CH4, and Their Binary Mixtures in Porous Organic Cage CC3. *J. Phys. Chem. C* **2019**, *123*, 24172−24180.
(70) Deshmane, C. A.; Jasinski, J. B.; Carreon, M. A. Microwave-Assisted Synthesis of Nanocrystalline Mesoporous Gallium Oxide. *Microporous Mesoporous Mater.* **2010**, *130*, 97−102.
(71) Zong, Z.; Carreon, M. A. Thin SAPO-34 membranes synthesized in stainless steel autoclaves for N_2/CH_4 separation. *Microporous Mesoporous Mater.* **2017**, *524*, 117−123.
(72) Lucero, J.; Osuna, C.; Crawford, J. M.; Carreon, M. A. Microwave-Assisted Synthesis of Porous Organic Cages CC3 and CC2. *CrystEngComm* **2019**, *21*, 4534−4537.
(73) Sing, K. S. W. Assessment of Surface Area by Gas Adsorption. In *Adsorption by Powders and Porous Solids: Principles, Methodology and Applications*, 2nd ed.; Elsevier Inc., 2013; pp 237−268.

https://doi.org/10.1021/acs.jpcc.1c04657
J. Phys. Chem. C 2021, 125, 20512−20521

(74) Ghorbani, H.; Ghahramaninezhad, M.; Niknam Shahrak, M. The Effect of Organic and Ionic Liquid Solvents on Structure Crystallinity and Crystallite Size of ZIF-8 for CO2 Uptake. *J. Solid State Chem.* **2020**, *289*, No. 121512.
(75) Lachance, J. *Investigation of Gas Hydrates Using Differential Scanning Calorimetry with Water-in-Oil Emulsions*; Colorado School of Mines: Golden, 2008.
(76) Gupta, A.; Lachance, J.; Sloan, E. D.; Koh, C. A. Measurements of Methane Hydrate Heat of Dissociation Using High Pressure Differential Scanning Calorimetry. *Chem. Eng. Sci.* **2008**, *63*, 5848−5853.
(77) Veluswamy, H. P.; Prasad, P. S. R.; Linga, P. Mechanism of Methane Hydrate Formation in the Presence of Hollow Silica. *Korean J. Chem. Eng.* **2016**, *33*, 2050−2062.
(78) Chari, V. D.; Sharma, D. V. S. G. K.; Prasad, P. S. R.; Murthy, S. R. Methane Hydrates Formation and Dissociation in Nano Silica Suspension. *J. Nat. Gas Sci. Eng.* **2013**, *11*, 7−11.
(79) Guo, Y.; Xiao, W.; Pu, W.; Hu, J.; Zhao, J.; Zhang, L. CH4 Nanobubbles on the Hydrophobic Solid-Water Interface Serving as the Nucleation Sites of Methane Hydrate. *Langmuir* **2018**, *34*, 10181−10186.
(80) Nguyen, N. N.; Galib, M.; Nguyen, A. V. Critical Review on Gas Hydrate Formation at Solid Surfaces and in Confined Spaces - Why and How Does Interfacial Regime Matter? *Energy Fuels* **2020**, *34*, 6751−6760.
(81) Bai, D.; Chen, G.; Zhang, X.; Sum, A. K.; Wang, W. How Properties of Solid Surfaces Modulate the Nucleation of Gas Hydrate. *Sci. Rep.* **2015**, *5*, No. 12747.
(82) Maeda, N. Interfacial Nanobubbles and the Memory Effect of Natural Gas Hydrates. *J. Phys. Chem. C* **2018**, *122*, 11399−11406.
(83) Hasell, T.; Schmidtmann, M.; Stone, C. A.; Smith, M. W.; Cooper, A. I. Reversible Water Uptake by a Stable Imine-Based Porous Organic Cage. *Chem. Commun.* **2012**, *48*, 4689−4691.
(84) Uchida, T.; Ebinuma, T.; Ishizaki, T. Dissociation Condition Measurements of Methane Hydrate in Confined Small Pores of Porous Glass. *J. Phys. Chem. B* **1999**, *103*, 3659−3662.
(85) Koh, C. A.; Wisbey, R. P.; Wu, X.; Westacott, R. E.; Soper, A. K. Water Ordering around Methane during Hydrate Formation. *J. Chem. Phys.* **2000**, *113*, 6390−6397.
(86) Kim, D.; Kim, D. W.; Lim, H.; Jeon, J.; Kim, H.; Jung, H.; Lee, H. Inhibited Phase Behavior of Gas Hydrates in Graphene Oxide: Influences of Surface and Geometric Constraints. *Phys. Chem. Chem. Phys.* **2014**, *16*, 22717−22722.
(87) Borchardt, L.; Nickel, W.; Casco, M.; Senkovska, I.; Bon, V.; Wallacher, D.; Grimm, N.; Krause, S.; Silvestre-Albero, J. Illuminating Solid Gas Storage in Confined Spaces-Methane Hydrate Formation in Porous Model Carbons. *Phys. Chem. Chem. Phys.* **2016**, *18*, 20607−20614.
(88) Slater, A. G.; Reiss, P. S.; Pulido, A.; Little, M. A.; Holden, D. L.; Chen, L.; Chong, S. Y.; Alston, B. M.; Clowes, R.; Haranczyk, M.; et al. Computationally-Guided Synthetic Control over Pore Size in Isostructural Porous Organic Cages. *ACS Cent. Sci.* **2017**, *3*, 734−742.
(89) Zhu, G.; Liu, Y.; Flores, L.; Lee, Z. R.; Jones, C. W.; Dixon, D. A.; Sholl, D. S.; Lively, R. P. Formation Mechanisms and Defect Engineering of Imine-Based Porous Organic Cages. *Chem. Mater.* **2018**, *30*, 262−272.
(90) Carreon, M. A.; Guliants, V. V. Macroporous Vanadium Phosphorus Oxide Phases Displaying Three-Dimensional Arrays of Spherical Voids. *Chem. Mater.* **2002**, *14*, 2670−2675.
(91) Breck, D. *Zeolite Molecular Sieves: Structure, Chemistry and Use*; John Wiley & Sons, Inc.: New York, 1974.
(92) Denning, S.; Majid, A. A. A.; Lucero, J. M.; Crawford, J. M.; Carreon, M. A.; Koh, C. A. Methane Hydrate Growth Promoted by Microporous Zeolitic Imidazolate Frameworks ZIF-8 and ZIF-67 for Enhanced Methane Storage. *ACS Sustainable Chem. Eng.* **2021**, *9*, 9001−9010.

https://doi.org/10.1021/acs.jpcc.1c04657
J. Phys. Chem. C 2021, 125, 20512−20521